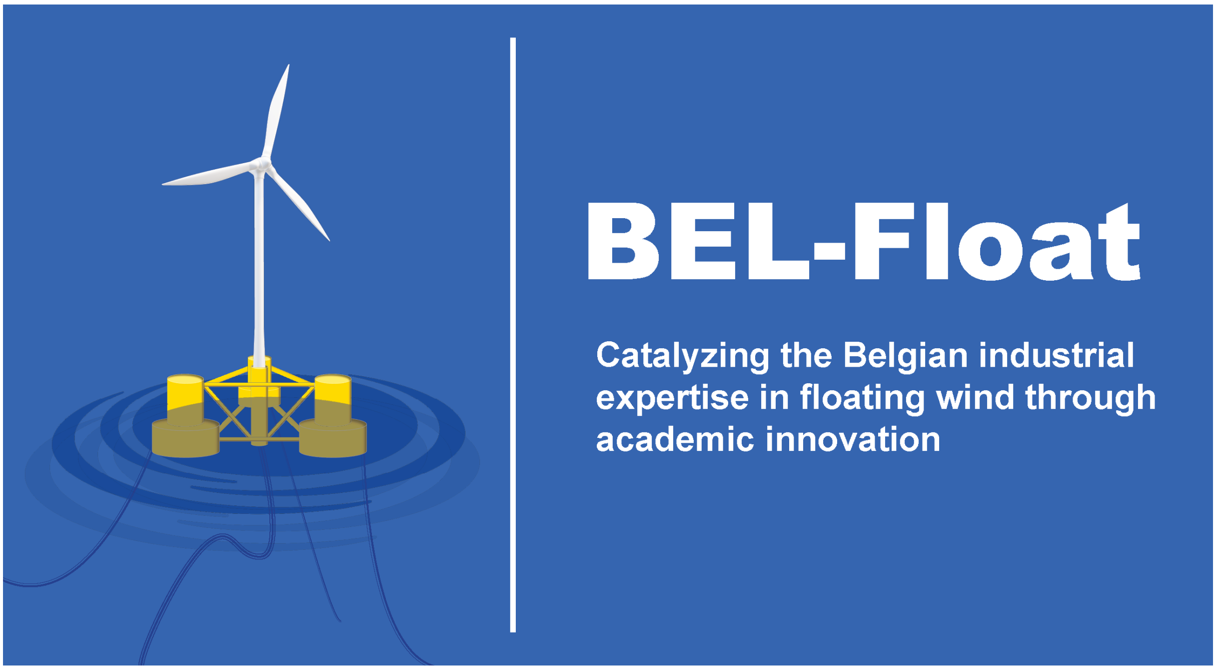

BEL-Float

Topic 5 - Fatigue lifetime of a FOW substructure

Deliverable 1 - Multi-dimensional modelling strategy

Date of delivery: 31/08/2024

Author: Ir.Victor Rappe
Review: Prof. Dr. Ir. Wim De Waele, Dr. Ing. Kris Hectors

University: Ghent University

Faculty: Faculty of Engineering and Architecture

Department: Department of Electromechanical, Systems and Metal Engineering

Research Group: Soete Laboratory

Financially supported by the FPS Economy (FOD Economie) under the call 2022 of the Energy Transition Fund.

Contents

1 Introduction **2**
1.1 Context within BEL-Float . . . 2
1.2 Problem statement . . . 2

2 Global shell-element model **3**
2.1 Definitions and inputs . . . 3
2.2 Hydrodynamic loads . . . 5
2.3 Hydrostatic loads . . . 7
2.4 Gravity and inertia loads . . . 8
2.5 Boundary conditions . . . 8

3 Solid element submodel **10**

4 Hot spot stress **10**

References **10**

1 Introduction

1.1 Context within BEL-Float

This report summarises the open-source multi-dimensional modelling strategy for calculating the local fatigue damage of welded joints based on a global dynamic analysis of a floating offshore wind turbine (FOWT). This represents the first deliverable (D1.1.5.1 - M10) for Topic 5 of the BEL-Float project.

The OC4 DeepCWind FOWT [1], illustrated in Figure 1, is used as a reference structure to develop this method. Hydrodynamic simulation results performed within the scope of Topic 1, performed in the open-source software OpenFAST v3.5.3 [2], serve as input for the method. The finite element (FE) solver Abaqus 2023 [3] is used for all structural simulations.

Figure 1: Illustration of the OC4 DeepCWind semi-submersible FOWT, as defined in [1]

1.2 Problem statement

Conducting a fatigue analysis of the substructure of a FOWT presents several challenges. In most dynamic modeling approaches, such as those used in software packages like OpenFAST, a flexible tower is coupled with a rigid substructure. This means that no internal forces and moments, and thus stresses, can be extracted from the substructure.

However, performing a detailed fatigue analysis of these critical regions, requires knowledge of local stresses. This necessitates the development of a FE model that considers the distributed pressure loads on the wetted surfaces due to waves and currents acting on the structure, rather than the resultant forces at the center of gravity (CoG) used in rigid body analyses. To address this, a method using a shell element model is developed, which will be explained in detail in Section 2. Note that this method is inspired by the works of Lee et al. [4] and Gao et al. [5].

After all loads have been applied on the shell element FE model, solid element submodels of fatigue critical locations will be used to consider the (local) effect of welds on the stress field. This will be discussed in Section 3. The results from these submodel simulations will then be used for a hot spot stress fatigue analysis to calculate the fatigue life of these critical regions, as elaborated in Section 4. A global overview of the multi-dimensional strategy can be found in Figure 2.

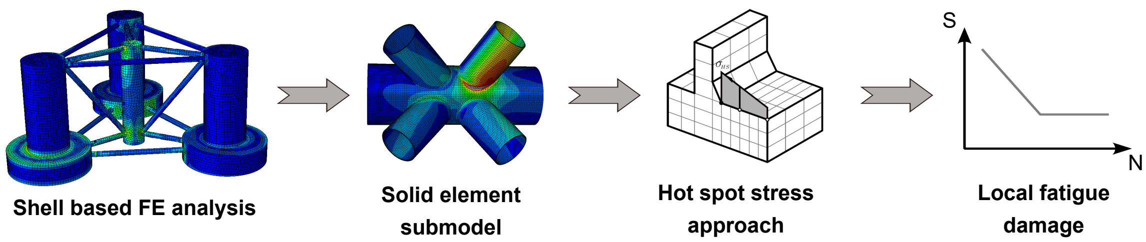

Figure 2: Global overview of the multi-dimensional modelling strategy

2 Global shell-element model

2.1 Definitions and inputs

A schematic overview of the shell element method is shown in Figure 3 and goes as follows. After a global hydrodynamic time domain analysis, the following outputs are extracted from this analysis and used as input to the method:

- the forces and moments at the transition piece between the tower and the floating platform;
- the forces at the mooring fairleads;
- the position and acceleration of the CoG of the floating platform in all six degrees of freedom (DoFs);
- the sea elevation at a reference point.

As all these inputs are considered in the global inertial reference frame used in the hydrodynamic simulation, an additional coordinate system has to be defined for the finite element model, as shown in Figure 4. The (X, Y, Z) coordinate system represents the global inertial reference frame used in the hydrodynamic simulation, while the (x, y, z) coordinate system has its origin as defined in [1], with $(0, 0, 0)$ at the intersection of the centre line of the central column and the waterline when the floater is in its neutral position.

The mooring line loads and tower bottom loads can be applied to the FE model after transforming them from the global (X, Y, Z) coordinate system to the local (x, y, z) coordinate system. However, for the hydrodynamic, hydrostatic, gravity, and inertia loads further processing of the input data is required. As a summary, all considered loads and their current implementation status are shown in Table 1.

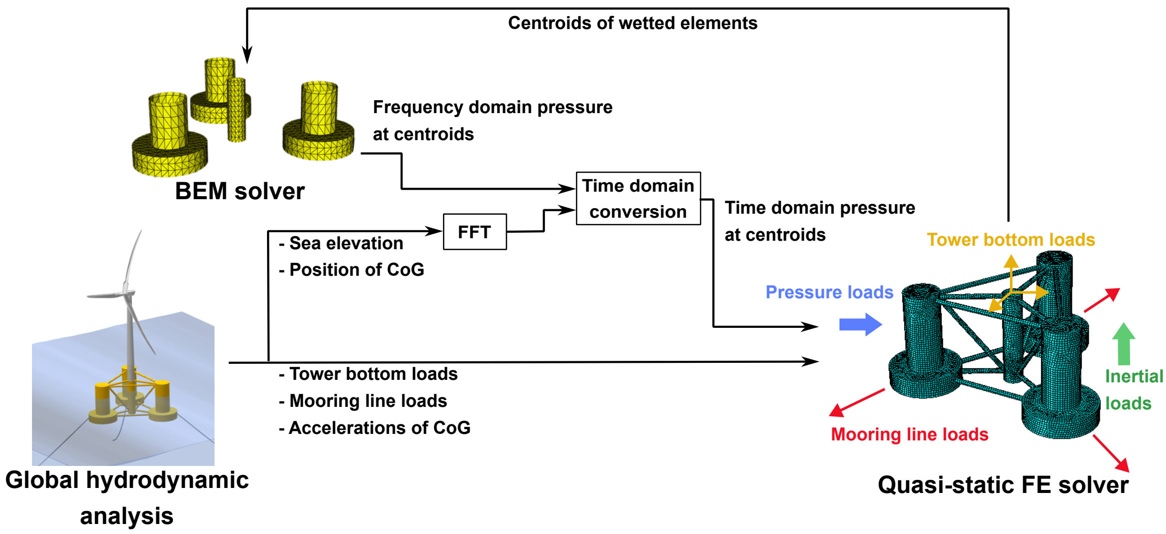

Figure 3: Schematic showing the method used to extract, calculate, and map the loads on an FE model

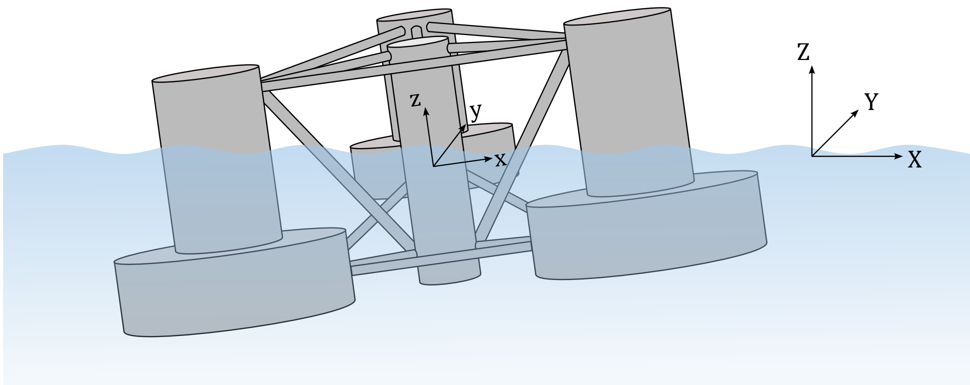

Figure 4: Illustration of coordinate systems used

Load Class	Load type
Concentrated loads	Tower base loads
	Mooring line loads
Hydrodynamic loads	Diffraction
	Radiation
	Froude-Krylov
	Morison drag term
Hydrostatic pressure	External wetted surface
	Ballast water
Body forces	Gravity loads floater
	Inertial loads floater
	Inertial loads ballast

Table 1: Summary of loads applied on FE model

2.2 Hydrodynamic loads

2.2.1 Pressure mapping method

To calculate the distributed Froude-Krylov, diffraction, and radiation pressures on the mean wetted surfaces of the floating structure, first a frequency domain simulation is conducted in Capytaine v2.2 [6], an open-source boundary element method (BEM) solver for linear potential flow. In this simulation complex pressure values across a range of frequencies are determined. Pressure values are calculated at the centroid of all wetted elements in the FE mesh for the Froude-Krylov loads ($p_{FK}(\omega, \text{centroid})$), diffraction loads ($p_{diffr}(\omega, \text{centroid})$), and all 6 DoFs of the radiation loads ($p_{FK}(\omega, \text{centroid}, \text{DoF})$). Since linear potential flow is considered, the BEM solver disregards the cross braces. Their slender shape allows to assume that their contributions are negligible [7].

To transform the frequency domain pressures into time domain data, the flowcharts shown in Figure 5 are followed. Note that no flowchart is given for the Froude-Krylov loads, as its calculation is completely analogous with the calculation of the diffraction loads. The flowchart for the diffraction problem will be explained in more detail hereunder.

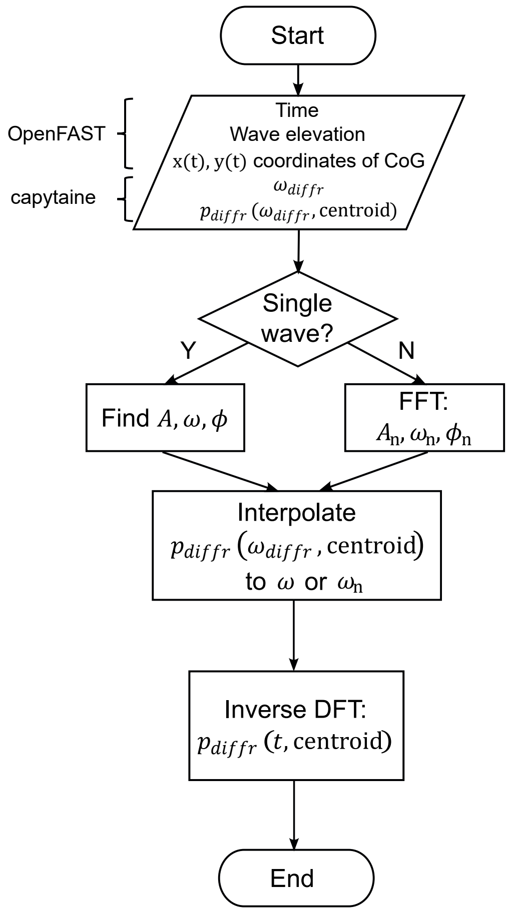

(a)

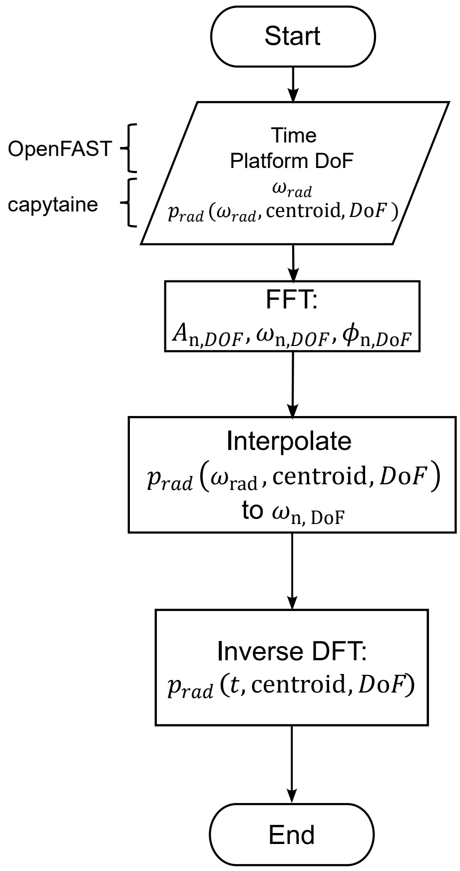

(b)

Figure 5: Flowcharts for calculating the time domain (a) diffraction and (b) radiation loads

For computational time optimisation, a distinction is made between simulations that consider a single wave and those that consider a wave spectrum. The wave elevation will be denoted as $h(t)$. The following steps are considered:

1. If a single wave is considered in the hydrodynamical simulation, its angular frequency ω, amplitude A, and phase angle ϕ are extracted from the signal $h(t)$.

   If a distributed wave is considered, it is assumed that the wave height $h(t)$ can be described as a finite Fourier series, i.e.:

$$h(t) = \Re\left[\sum_{n=1}^{N} A_n e^{i(\omega_n t+\phi_n)}\right] \tag{1}$$

   with N the number of frequencies, and A_n and ϕ_n respectively the amplitude and phase angle corresponding to the angular frequency ω_n. A Fast Fourier transform (FFT) is used to extract the amplitudes h_n, angular frequencies ω_n, and phase angles ϕ_n from $h(t)$.

2. As the angular frequencies used in the BEM solver and the angular frequency/frequencies $\omega_{(n)}$ calculated for the single wave or by the FFT are not necessarily equal, $p_{diffr}(\omega_{\text{diffr}}, \text{centroid})$ is interpolated to $p_{diffr}(\omega_{(n)}, \text{centroid})$, with ω_{diffr} the range of frequencies considered in the BEM solver. Note that as a linear problem is considered, the complex pressure values $p_{diffr}(\omega_n, \text{centroid})$ of the wave spectrum can be regarded as a discrete transfer function.

3. The time domain diffraction pressure $p_{\text{diffraction}}(t, \text{centroid})$ for a single wave is then determined via:

$$p_{\text{diffr}}(t, \text{centroid}) = \Re\left[A\, p_{\text{diffr}}(\omega, \text{centroid}) e^{i(\omega t+\phi)} e^{ikXY(t)}\right] \tag{2}$$

   and for a wave spectrum via an inverse discrete Fourier transform (DFT):

$$\begin{aligned} p_{\text{diffr}}(t, \text{centroid}) = \Re\Bigg[&\frac{1}{N} A_0\, p_{\text{diffr}}(0, \text{centroid}) e^{i\phi_0} \\ &+ \frac{2}{N}\sum_{n=1}^{N} A_n\, p_{\text{diffr}}(\omega_n, \text{centroid}) e^{i(\omega_n t+\phi_n)} e^{ik_n XY(t)}\Bigg] \end{aligned} \tag{3}$$

   with wave number $k_{(n)}$, and $XY(t) = X(t)\cos(\beta) + Y(t)\sin(\beta)$, where $X(t)$ and $Y(t)$ are, respectively, the X and Y coordinates of the floater in the global reference frame during the hydrodynamical simulation and β is the wave direction. The term $e^{ik_{(n)}XY(t)}$ is a phase correction to accommodate the movement of the floater in the time domain. Note that for the first part of Eq. 3, $\omega_0 = 0\,\text{rad/s}$ and $k_0 = 0\,\text{m}^{-1}$.

The calculation of the radiation pressures goes similarly, with two main differences:

- No distinction is made for the single wave case, as the movement of the platform will never be perfectly sinusoidal due to transient effects.
- The time domain pressure is now also a function of the considered DoF and is given by:

$$\begin{aligned} p_{rad}(t, centroid, DoF) =& \Re\Bigg[\frac{1}{N} A_0 p_{rad}(0, centroid, DoF) e^{i\phi_0} \\ &+ \frac{2}{N}\sum_{n=1}^{N} A_n p_{rad}(\omega_n, centroid, DoF) e^{i(\omega_n t+\phi_n)}\Bigg] \end{aligned} \tag{4}$$

Note that the phase correction $k_n XY(t)$ is not present when calculating the time domain pressure, as the radiation loads only consider the movement of the platform and not the local wave elevation.

As mentioned above, these time domain pressures are determined for the centroid of each wetted shell element of the FE mesh. By summing up the contributions of the diffraction, Froude-Krylov and radiation pressures and assigning them to their corresponding element, a distributed pressure field is created on the FE model. Note that this permits the use of different meshes for the BEM and FE analyses.

2.2.2 Morison loads

To incorporate the effect of drag on the dynamics of the platform, the drag term of the Morison equation [8] (Eq. 5) is included on all submerged members of the substructure in the hydrodynamic simulation. Note that this includes both the submerged cylindrical members and the heave plates.

$$F_{drag} = \frac{1}{2}\rho C_d A u|u| \tag{5}$$

with ρ the fluid density, C_d the drag coefficient, A the projected surface perpendicular to the flow velocity, and u the relative fluid velocity on the member.

To get accurate drag loads on the FE model, it would be best to have distributed drag loads over the length of all submerged members. However, OpenFAST only allows to extract these forces "at up to nine locations for up to nine different members, for a total of 81 possible local member output locations" [9]. As the considered platform has more than nine members, the source code of the Hydrodyn module of OpenFAST is altered to accommodate these extra members.

Still the forces can only be extracted for a maximum of nine locations per member, which means that these locations must be carefully selected. According to Airy wave theory, fluid velocity decays exponentially with depth [10], so the points will be chosen non-uniformly over the depth. This approach is similar to that used by Diogo [11], as shown in Figure 6. Since this part of the strategy is still under development at the time of writing, the final distribution has yet to be determined.

2.3 Hydrostatic loads

As the hydrodynamic simulation considers rigid body dynamics and small movements, the hydrostatic loads on the mean external wetted surfaces are evaluated as a hydrostatic restoring matrix around the CoG. In other words, the effect of the changing instantaneous wetted surface on the hydrostatic pressure is not considered. The proposed method will improve this by considering the hydrostatic pressure up until the instantaneous mean water line as shown in Figure 7a.

For the hydrostatic pressure of the ballast water, a similar approach is used. While the hydrodynamic simulation considers the ballast as point masses, a distributed hydrostatic load is applied in the finite element model, which changes as function of the orientation of the floater. Note that as the "[ballast] water is compartmentalized and is not allowed to move or slosh" [1], a pressure profile as shown in Figure 7b is applied to the finite element model.

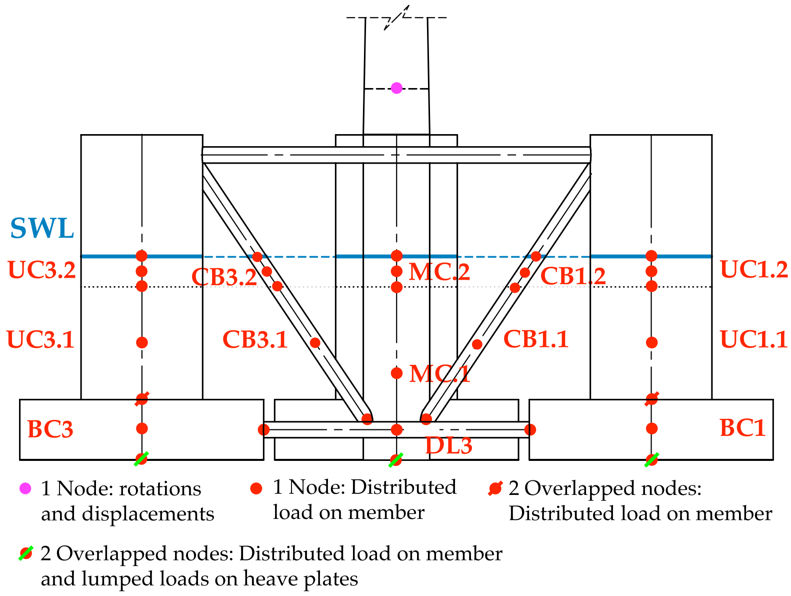

Figure 6: Distribution of points where Morison forces are extracted, as used in the work of Diogo [11]

2.4 Gravity and inertia loads

A gravity load is added to the light weight of the floater (i.e. the steel weight). The gravity load of the ballast water is already included in the model due to the hydrostatic loads. Similar to the hydrostatic loads, the gravity loads are applied in such a way that the gravity is oriented in the negative Z-direction in the global coordinate system (X, Y, Z).

For the inertial loads, again a distinction is made between the light weight of the floater and the ballast. By using the (rotational) accelerations of the CoG from the hydrodynamic analysis, the inertial loads of the light weight can be directly added on the FE model. The ballasts are this time considered as point masses and their accelerations are calculated using Eq. 6, with $\boldsymbol{a}_{CoG}$, $\boldsymbol{\omega}$, and $\boldsymbol{\alpha}$ the acceleration, angular velocity, and angular acceleration of the CoG in the (X, Y, Z) coordinate system, and $\boldsymbol{r}_{ballast|CoG}$ the vector between the ballast and CoG in the (x, y, z) coordinate system. The inertial loads $(m_{ballast}\boldsymbol{a}_{ballast})$ are then applied to the FE model using a continuum distributing coupling.

$$\boldsymbol{a}_{\text{ballast}} = \boldsymbol{a}_{CoG} + \boldsymbol{\alpha} \times \boldsymbol{r}_{ballast|CoG} + \boldsymbol{\omega} \times (\boldsymbol{\omega} \times \boldsymbol{r}_{ballast|CoG}) \tag{6}$$

2.5 Boundary conditions

Due to numerical errors and differences in how hydrostatic loads are modeled in the FE model compared to the hydrodynamic model, force equilibrium cannot be guaranteed in the FE model. Since the primary focus is on the stresses in the regions around the welds, the translational DoFs at the centers of the bottoms of the three heave plates will be constrained as fixed-fixed-fixed, free-fixed-fixed, and free-free-fixed respectively in the (x, y, z) coordinate system.

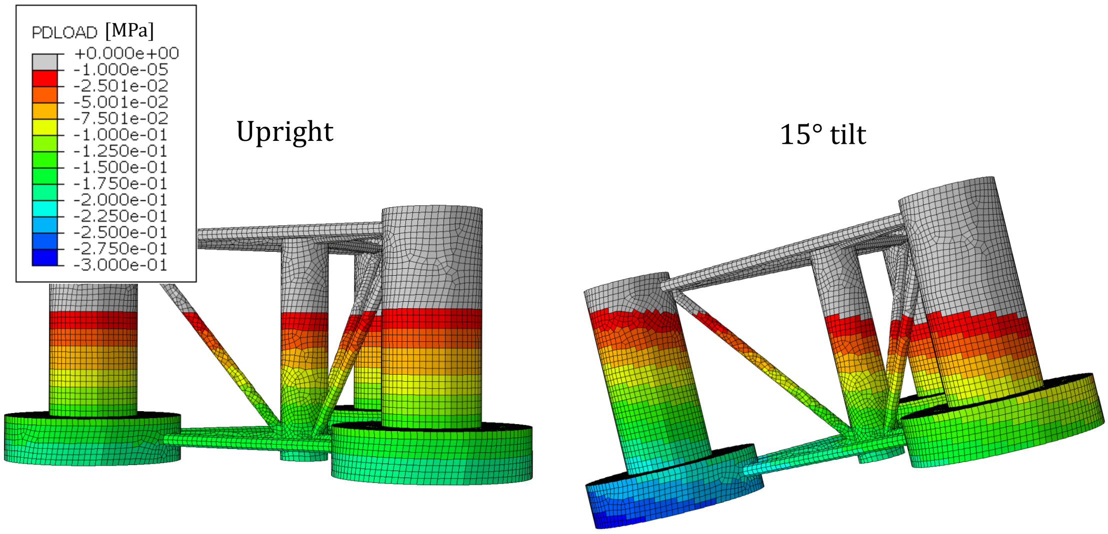

(a)

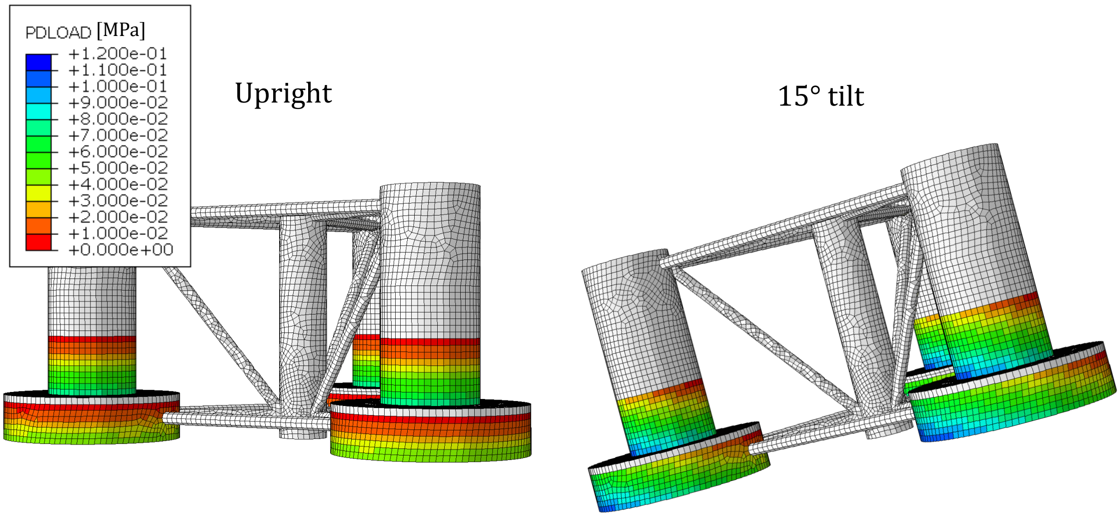

(b)

Figure 7: Modelling strategy of the hydrostatic pressure of (a) the external wet surface and (b) the ballast water

3 Solid element submodel

Due to the presence of welds, eight fatigue critical locations can be identified. Solid elements submodels will be made from each of these locations. These are shown in Figure 8. For these submodels subsequent steps will be followed:

1. Determine the appropriate size of the submodel. It should be large enough that the stresses in the area of interest are not influenced by the boundary conditions (Saint-Venant's principle), but as small as possible to reduce the computational load. This will be done iteratively on a solid element submodel on which the weld is not included.

2. Model and mesh the weld on the solid element submodel.

3. Couple the solid element submodel with the global shell element model.

4. Introduce hydrostatic and -dynamic pressures on the submerged submodels.

5. Solve the submodel.

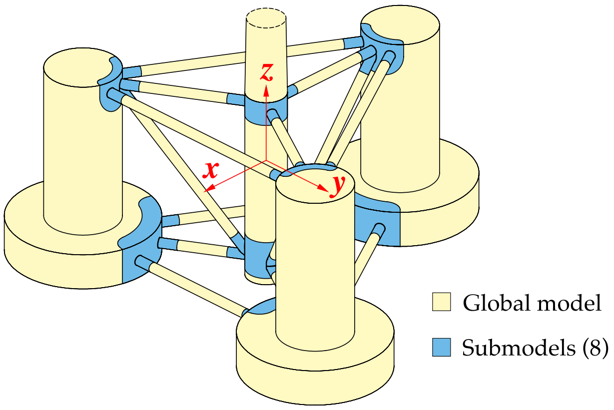

Figure 8: Schematic overview of possible locations for submodels [11]

4 Hot spot stress

The fatigue life will be calculated based on the structural (hot spot) stress approach. The fatigue governing stress spectra will be extracted from the FE submodel based on the in-house created method of Hectors et al. [12][13]. The rainflow counting method combined with the Palmgren-Miner damage rule will then be employed to determine the local fatigue damage.

References

[1] A. Robertson, J. Jonkman, M. Song, A. Goupee, A. Coulling, C. Luan, Definition of the semisubmersible floating system for phase ii of oc4, 2014. URL: `https://www.nrel.gov/docs/fy14osti/60601.pdf`.

[2] J. Jonkman, Openfast, 2023. URL: https://www.nrel.gov/wind/nwtc/openfast.html.

[3] Dassault Systèmes, 2024. URL: https://www.3ds.com/products/simulia/abaqus.

[4] D. C. Lee, S. kwon Na, S. Kim, C. wan Kim, Deterministic fatigue damage evaluation of semi-submersible platform for wind turbines using hydrodynamic-structure interaction analysis, International Journal of Precision Engineering and Manufacturing - Green Technology 9 (2022) 1317–1328. URL: https://link.springer.com/article/10.1007/s40684-021-00326-7. doi:10.1007/S40684-021-00326-7/TABLES/5.

[5] Z. Gao, D. Merino, K. J. Han, H. Li, S. Fiskvik, Time-domain floater stress analysis for a floating wind turbine, Journal of Ocean Engineering and Science 8 (2023) 435–445. doi:10.1016/J.JOES.2023.08.001.

[6] M. Ancellin, A python-based linear potential flow bem solver, 2022. URL: https://capytaine.github.io/stable/.

[7] A. Pribadi, L. Donatini, E. Lataire, G. V. Fernandez, I. Martínez-Estévez, Validation of a computationally efficient time-domain numerical tool against DeepCwind experimental data, in: Trends in Renewable Energies Offshore, 1 ed., CRC Press, London, 2022, pp. 597–608. URL: https://www.taylorfrancis.com/books/9781003360773/chapters/10.1201/9781003360773-68. doi:10.1201/9781003360773-68.

[8] J. Morison, J. Johnson, S. Schaaf, The force exerted by surface waves on piles, Journal of Petroleum Technology 2 (1950) 149–154. doi:10.2118/950149-g.

[9] J. Jonkman, Openfast documentation, 2023. URL: https://openfast.readthedocs.io/en/dev/.

[10] S. Chakrabarti, Hydrodynamics of offshore structures, Computational Mechanics Publications, 1987.

[11] R. D. Diogo, Analysis of the structural integrity of a floating semisubmersible foundation for offshore wind (2017).

[12] K. Hectors, H. De Backer, M. Loccufier, W. De Waele, Numerical framework for fatigue lifetime prediction of complex welded structures, Frattura ed Integrita Strutturale 14 (2020) 552–566. doi:10.3221/IGF-ESIS.51.42.

[13] K. Hectors, W. De Waele, A numerical framework for determination of stress concentration factor distributions in tubular joints, International Journal of Mechanical Sciences 174 (2020) 105511. doi:10.1016/J.IJMECSCI.2020.105511.